



## Article

# Construction of Chemically Bonded Interface of Organic/Inorganic g-C<sub>3</sub>N<sub>4</sub>/LDH Heterojunction for Z-Schematic Photocatalytic H<sub>2</sub> Generation

Yuzhou Xia <sup>1</sup>, Ruowen Liang <sup>1</sup>, Min-Quan Yang <sup>2,\*</sup> , Shuying Zhu <sup>3,\*</sup> and Guiyang Yan <sup>1,4,\*</sup>

<sup>1</sup> Fujian Province University Key Laboratory of Green Energy and Environment Catalysis, Ningde Normal University, Ningde 352100, China; yzxia@ndnu.edu.cn (Y.X.); t1629@ndnu.edu.cn (R.L.)

<sup>2</sup> Fujian Key Laboratory of Pollution Control & Resource Reuse, College of Environmental Science and Engineering, Fujian Normal University, Fuzhou 350007, China

<sup>3</sup> College of Chemistry, Fuzhou University, Fuzhou 350116, China

<sup>4</sup> Provincial Key Laboratory of Featured Materials in Biochemical Industry, Ningde Normal University, Ningde 352100, China

\* Correspondence: yangmq@fjnu.edu.cn (M.-Q.Y.); syzhu@fzu.edu.cn (S.Z.); ygyfjnu@163.com (G.Y.)

**Abstract:** The design and synthesis of a Z-schematic photocatalytic heterostructure with an intimate interface is of great significance for the migration and separation of photogenerated charge carriers, but still remains a challenge. Here, we developed an efficient Z-scheme organic/inorganic g-C<sub>3</sub>N<sub>4</sub>/LDH heterojunction by in situ growing of inorganic CoAl-LDH firmly on organic g-C<sub>3</sub>N<sub>4</sub> nanosheet (NS). Benefiting from the two-dimensional (2D) morphology and the surface exposed pyridine-like nitrogen atoms, the g-C<sub>3</sub>N<sub>4</sub> NS offers efficient trap sites to capture transition metal ions. As such, CoAl-LDH NS can be tightly attached onto the g-C<sub>3</sub>N<sub>4</sub> NS, forming a strong interaction between CoAl-LDH and g-C<sub>3</sub>N<sub>4</sub> via nitrogen–metal bonds. Moreover, the 2D/2D interface provides a high-speed channel for the interfacial charge transfer. As a result, the prepared heterojunction composite exhibits a greatly improved photocatalytic H<sub>2</sub> evolution activity, as well as considerable stability. Under visible light irradiation of 4 h, the optimal H<sub>2</sub> evolution rate reaches 1952.9 μmol g<sup>-1</sup>, which is 8.4 times of the bare g-C<sub>3</sub>N<sub>4</sub> NS. The in situ construction of organic/inorganic heterojunction with a chemical-bonded interface may provide guidance for the designing of high-performance heterostructure photocatalysts.



**Citation:** Xia, Y.; Liang, R.; Yang, M.-Q.; Zhu, S.; Yan, G. Construction of Chemically Bonded Interface of Organic/Inorganic g-C<sub>3</sub>N<sub>4</sub>/LDH Heterojunction for Z-Schematic Photocatalytic H<sub>2</sub> Generation. *Nanomaterials* **2021**, *11*, 2762. <https://doi.org/10.3390/nano11102762>

Academic Editors: Protima Rauwel and Erwan Rauwel

Received: 25 September 2021

Accepted: 14 October 2021

Published: 18 October 2021

**Publisher's Note:** MDPI stays neutral with regard to jurisdictional claims in published maps and institutional affiliations.



**Copyright:** © 2021 by the authors. Licensee MDPI, Basel, Switzerland. This article is an open access article distributed under the terms and conditions of the Creative Commons Attribution (CC BY) license (<https://creativecommons.org/licenses/by/4.0/>).

**Keywords:** chemically bonded interface; heterojunction; Z-scheme; g-C<sub>3</sub>N<sub>4</sub>/LDH; photocatalytic

## 1. Introduction

The worsening environmental pollution and energy crisis caused by the large-scale consumption of fossil fuels has posed a great threat to the sustainable development of mankind. Solar-driven photocatalytic H<sub>2</sub> evolution is deemed to be a promising approach to meet the challenges, due to the easy accessibility and renewability of solar energy [1–7]. Since the first report of photoelectrochemical water splitting over a TiO<sub>2</sub> electrode by Fujishima and Honda, diverse catalysts have been developed for photocatalytic H<sub>2</sub> evolution, including TiO<sub>2</sub> [8–12], g-C<sub>3</sub>N<sub>4</sub> [13–15], ZnIn<sub>2</sub>S<sub>4</sub> [16,17], COFs [18], MOFs [19–21] and so on. However, despite much progress being made in the area, the overall efficiency is still much less than satisfactory, owing to some stubborn issues, such as insufficient light harvesting and fast recombination of photogenerated electron–hole pairs.

Over the past decades, the construction of heterostructure, especially for Z-scheme heterostructure, is an effective strategy to mediate these problems [22–31]. In such a system, the photogenerated electrons and holes are spatially separated to the component with a more negative conduction band (CB) position and the counterpart with more positive valence band (VB) position, respectively. This not only benefits the light utilization and boosts the separation of photogenerated charge carriers, but also maintains the high redox

ability of the charge carriers. In order to construct an efficient Z-scheme photocatalyst, it is necessary to design a high-quality junction with matched band structures and Fermi energy levels ( $E_f$ ) between two components to drive the migration of electrons–holes, as well as a compactly bonded interface to facilitate the charge transfer across the boundary. Currently, great efforts have been devoted to the design of band-aligned heterojunction systems. Relative mature guiding principles are formed. However, less attention has been paid to the interfacial engineering [32–34]. Most of the reported heterojunctions are mixtures of two components with weak interaction through Van der Waals forces. As such, photogenerated electrons and holes are easily accumulated and recombined at the interface.

Very recently, the construction of strong interacted interfaces connected via chemical bonds have provided an insight for optimizing the charge migration in terms of efficiency and accuracy, thereby improving the photocatalytic  $H_2$  evolution performance. For example, Li et al. reported the synthesis of a Mo-S bonded Z-scheme heterojunction by in situ growth of  $MoSe_2$  on  $ZnIn_2S_4$  nanosheets with an S defect [35]. The  $MoSe_2$ – $ZnIn_2S_4$  demonstrates a greatly improved  $H_2$  generation rate than pristine  $ZnIn_2S_4$ . Nevertheless, most of the developed chemical-bond-linked heterostructures are all-inorganic systems, which suffer from limitations such as the difficulty in creating anchoring sites for growing the other semiconductor component, and the instability of the surface coordinative unsaturated atoms [36–38]. In this context, inspired by the efficient electron transfer of bio-enzyme systems in nature, which are composed of an inorganic metal center and organic coenzyme through the coordination of metal and protein, the construction of organic/inorganic hybrids may be a more convenient and universal approach to obtain strong interacted heterojunctions.

$g-C_3N_4$  is expected to be a promising organic support due to a good coordination ability, as well as appropriate band-edge positions and high visible light absorption. Especially, an ultrathin 2D  $g-C_3N_4$  NS is rich in pyridine-like nitrogen atoms, which can coordinate with metal precursors via strong nitrogen–metal interaction, yielding a chemical-bonded interface [39–41]. As for the inorganic counterpart, we focus on the layered double hydroxides (CoAl-LDHs) due to the large exposure of transition metal atoms. As such, herein, we purposely design and synthesize an organic/inorganic  $g-C_3N_4$ /CoAl-LDH heterojunction with a chemical-bond-connected interface for efficient photocatalytic  $H_2$  generation. The structure, morphology and photoabsorption properties of the prepared samples are characterized in detail. Photocatalytic activity test results reveal that the heterojunction composites show a much higher  $H_2$  evolution rate than pure  $g-C_3N_4$  NS under visible light irradiation. Collective photoelectrochemical characterizations disclose that the excellent photocatalytic behavior can be attributed to the intimate interface with a sufficient contact area, which endows the heterojunction with more high-speed channels for the migration of charge carriers.

## 2. Materials and Methods

### 2.1. Materilas

All reagents were analytical grade and used without further purification. Urea,  $Co(NO_3)_2$ ,  $Al(NO_3)_3$ , and  $NH_4F$  were purchased from Sinopharm Chemical Reagent Co., Ltd. (Beijing, China).

### 2.2. Preparation of Catalyst

Fabrication of  $g-C_3N_4$  NS: Bulk  $g-C_3N_4$  was firstly synthesized by annealing urea (10 g) at 550 °C for 4 h at the rate of 2.3 °C  $min^{-1}$  in air. The obtained sample was ground into power. Then, 1 g bulk  $g-C_3N_4$  power was added into 50 mL  $H_2O$  and ethyl alcohol with a volume ratio of 1:1 and sonicated for 2 h. The resultant suspension was centrifuged at 3500 rpm for 10 min to remove the residual layered precursor. Consequently, a  $g-C_3N_4$  NS suspension with a concentration of  $\sim 2$  mg  $mL^{-1}$  was obtained, denoted as CN.

Organic/inorganic  $g-C_3N_4$ /CoAl-LDH heterojunction was synthesized by in situ growth of CoAl-LDH onto  $g-C_3N_4$  NS. Typically, 0.25 mmol  $Co(NO_3)_2$ , 0.125 mmol

$\text{Al}(\text{NO}_3)_3$ , 4 mmol urea and 8 mmol  $\text{NH}_4\text{F}$  were added into the g- $\text{C}_3\text{N}_4$  NS suspension (50 mL) under vigorous stirring for 30 min. The mixture was heated at 120 °C in a Teflon-lined autoclave for 12 h, then cooled to room temperature naturally. The obtained precipitation was centrifuged and washed with deionized water several times and dried in a vacuum oven overnight at 60 °C, denoted as CN-CoAl<sub>0.25</sub>. A series of g- $\text{C}_3\text{N}_4$ /CoAl-LDH heterojunctions were prepared by varying the amounts of CoAl-LDH precursors via the same synthesis method, and were named as CN-CoAl<sub>x</sub>. For comparison, pure CoAl-LDH was synthesized via the same method without the addition of g- $\text{C}_3\text{N}_4$  NS.

### 2.3. Characterization

The as-prepared samples were characterized by powder X-ray diffraction (XRD) on a Bruker D8 Advance X-ray diffractometer (Bruker AXS GmbH, Karlsruhe, Germany), operated at 40 kV and 40 mA with Ni-filtered Cu K irradiation ( $\lambda = 1.5406 \text{ \AA}$ ). The Fourier-transform infrared (FTIR) spectra were carried out on a Nicolet 670 FTIR spectrometric analyzer (Thermo Electron, Waltham, MA, USA). UV-vis diffuse reflectance spectra (UV-vis DRS) were obtained by using a UV-vis spectrophotometer (Varian Cary 500, Varian, CA, America). The morphologies of the products were observed by scanning electron microscopy (FEI Nova NANO-SEM 230 spectrophotometer, Hillsboro, OR, USA). Transmission electron microscopy (TEM) images were obtained using a JEOL model JEM 2010 EX instrument (JEOL, Tokyo, Japan) at an accelerating voltage of 200 kV. X-ray photoelectron spectroscopy (XPS) measurements were carried out by using a VG Scientific ESCA Lab Mark II spectrometer (VG Scientific Ltd., Manchester, UK), equipped with two ultra-high vacuum 6 (UHV) chambers. The binding energies of all tested samples were calibrated by C 1s at 284.6 eV. BET surface area tests were performed on an ASAP2020M apparatus (Micromeritics Instrument Corp., Atlanta, GA, USA). Electron paramagnetic resonance (EPR) spectroscopic measurements were tested via Bruker A300 EPR spectrometer (Bruker AXS GmbH, Karlsruhe, Germany). Raman spectra were recorded on a Renishaw Raman spectrometer (Renishaw InVia, Gloucestershire, UK) with a laser beam of  $\lambda = 325 \text{ nm}$ . PL was measured by a fluorophotometer (Edinburgh FLS1000, Edinburgh Instruments, Livingston, UK) with an excitation wavelength of 375 nm.

### 2.4. Electrochemistry Measurement

The working electrode was prepared on fluorine-doped tin oxide (FTO) glass, which was cleaned by sonication in acetone and ethanol for 30 min, and 5 mg of the as-prepared samples were dispersed in 0.5 mL N, N-dimethylformamide under sonication for 2 h. Additionally, 10  $\mu\text{L}$  of slurry was dip coated onto the FTO side with exposed areas of 0.25  $\text{cm}^2$ . The uncoated parts of the FTO electrodes were sealed with epoxy resin. The electrochemical measurements were performed in a conventional three-electrode cell, using a Pt plate and an Ag/AgCl electrode as a counter electrode and reference electrode, respectively. The working electrode was immersed in a 0.2 M  $\text{Na}_2\text{SO}_4$  aqueous solution for 40 s before measurement. The photocurrent measurement was conducted with a CHI650E electrochemical workstation (Chenhua Instruments, Shanghai, China). Electrochemical impedance spectroscopy (EIS) was recorded on a ZENNIUM IM6 electrochemical workstation (Zahner, Germany). A 300 W Xe lamp (PLS-SXE300C, Perfectlight Co., Beijing, China) was used as a light source.

### 2.5. Evaluation of Photocatalytic Activity

The photocatalytic  $\text{H}_2$  evolution activity was evaluated in a Pyrex top-irradiation-type reaction vessel connected to a glass-closed gas circulation system. In the typical photocatalytic experiment, 40 mg photocatalyst with 40  $\mu\text{L}$  of 10  $\text{mg mL}^{-1}$   $\text{H}_2\text{PtCl}_6 \cdot 6\text{H}_2\text{O}$  were added into 50 mL solution with 10% triethanolamine (TEOA), which acted as sacrificial agent to trap the photogenerated holes. The suspension was vacuum treated for 30 min to eliminate the air. A 300 W Xenon lamp (PLS-SXE300C, Perfectlight Co., Beijing, China)

equipped with a 420 nm cut-off filter was used as the light source. H<sub>2</sub> was detected using an online gas chromatograph (Tianmei, TCD, Ar carrier, Shanghai, China).

### 3. Results and Discussion

Figure 1a schematically illustrates the synthesis of the organic/inorganic g-C<sub>3</sub>N<sub>4</sub>/CoAl-LDH heterojunction. Bulk g-C<sub>3</sub>N<sub>4</sub> was ultrasonically exfoliated into 2D nanosheets, firstly. Then, the nanosheets were employed as an organic support to mix with the LDH precursor for hydrothermal treatment, which enabled the in situ growth of CoAl-LDH onto the CN, forming 2D/2D heterojunction. Figure 1b depicts the XRD patterns of the as-prepared samples. Two typical diffraction peaks at 13° and 27° were observed in CN, associated with the trigonal N linkage of tri-s-triazine motifs (100) and periodic stacking of layers for conjugated aromatic systems (001), respectively. For pure CoAl-LDH, all of the peaks can be well indexed to a hexagonal CoAl-LDH phase (JCPDS NO. 51-0045). The diffraction peaks at 11.5°, 23.3°, 34.4°, 38.9° and 46.5° corresponded to the (003), (006), (012), (015) and (018) lattice planes of CoAl-LDH, respectively. In case of CN-CoAl<sub>x</sub> samples, both characteristic peaks of CN and CoAl-LDH were observed. The peak intensity of LDH increased gradually with the increment in CoAl-LDH content, demonstrating the successful integration of the two components in the heterojunction.

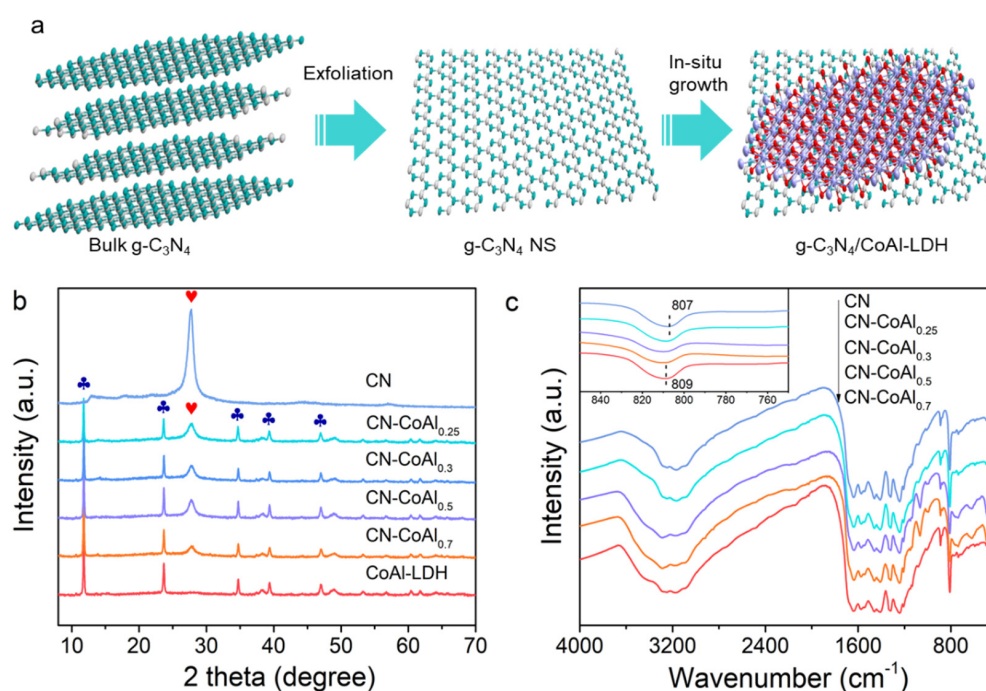


**Figure 1.** Schematic illustration of preparation of g-C<sub>3</sub>N<sub>4</sub>/CoAl-LDH heterojunction (a), XRD patterns (b) and FTIR spectra (c) of the as-prepared samples.

The chemical structure of the nanocomposites was investigated by FTIR analysis, as shown in Figure 1c. In comparison with CN, the FTIR spectra of CN-CoAl<sub>x</sub> showed similar characteristic peaks in the range of 900–1700 cm<sup>-1</sup> assigned to the stretching vibrations of tri-s-triazine heterocyclic rings [42], validating the preservation of the major chemical structure of g-C<sub>3</sub>N<sub>4</sub> in the heterojunction. As can be seen from the enlarged inset in Figure 1c, the peak at 807 cm<sup>-1</sup> ascribing to the breathing vibration of tri-s-triazine showed a gradual shift towards a higher wavenumber, with the increasing amount of CoAl-LDH in the composites. The corresponding peak shifted to 809 cm<sup>-1</sup> for CN-CoAl<sub>0.7</sub> suggested a strong chemical interaction between CN and CoAl-LDH in the heterojunction.

Figure 2 shows the SEM and TEM images of the CN, CoAl-LDH and CN-CoAl<sub>0.5</sub>, which were employed to analyze the micromorphology and structure information of the samples. As shown in Figure 2a, pure CN exhibited a typical 2D layered structure

composed of ultrathin nanosheets. CoAl-LDH (Figure 2b) displayed a nanoflower assembly structure of nanosheets. As for CN-CoAl<sub>0.5</sub>, the characteristic nanosheet structure of CN was observed (Figure 2c). However, no obvious LDH nanoflower could be detected. This might have been caused by the CN nanosheets that assisted the in situ growth of the CoAl-LDH, which promoted the dispersion of the LDH and inhibited its aggregation. When it further increased the loading amount of CoAl-LDH onto g-C<sub>3</sub>N<sub>4</sub>, both the characteristic structure of CN and CoAl-LDH were observed (Supplementary Materials, Figure S1). The excessive loading of the CoAl-LDH caused the self-aggregation. Figure 2d–f displays the TEM images of the CN-CoAl<sub>0.5</sub>. It is obvious that the heterojunction displayed a sheet-on-sheet structure with planar interface, which is conducive for the high flow and fast transference of charges, due to the large contact interface and excellent electron mobility [43]. HRTEM analysis revealed obvious lattice fringes of 0.26 nm that are assigned to the (012) facets of CoAl-LDH [44]. Meanwhile, an amorphous CN was observed to attach closely to the CoAl-LDH, suggesting a good interfacial contact between the two components. EDS elemental mappings of CN-CoAl<sub>0.5</sub> presented the co-existence of C, N, Co, Al and O, further validating the formation of a heterojunction structure.

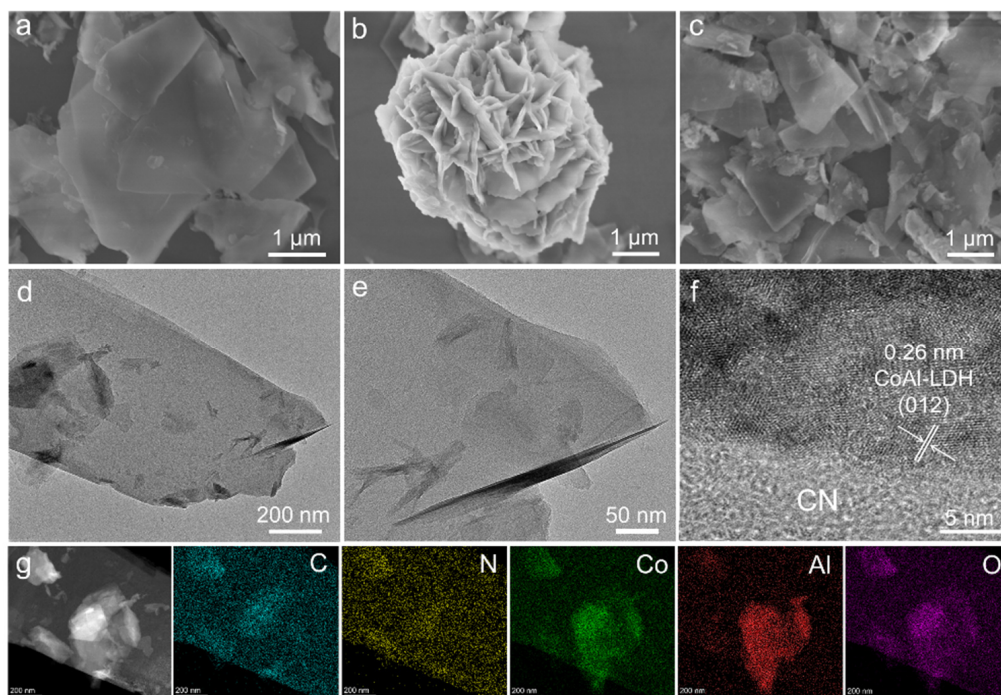


**Figure 2.** SEM images of CN (a), CoAl-LDH (b), CN-CoAl<sub>0.5</sub> (c), TEM of CN-CoAl<sub>0.5</sub> (d–f) and the corresponding EDS element mappings (g).

Moreover, the composition and chemical state of the as-prepared samples were measured by XPS. Both elements of CN and CoAl-LDH existed in the CN-CoAl<sub>0.5</sub> (Figure 3a), verifying the integration of CN with CoAl-LDH. For the C 1s spectrum of CN (Figure 3b), two peaks located at the binding energies of 284.6 and 288.0 eV were detected, which corresponded to the sp<sup>2</sup> C-C and N-C=N units, respectively. In comparison, the C 1s of CN-CoAl<sub>0.5</sub> could be fitted into three peaks at 284.6, 287.9 and 289.5 eV. The new peak at 289.5 eV could be attributed to C=O, which was generated from the hydrolysis of urea in the synthesis of CoAl-LDH [44]. The N 1s spectrum of CN-CoAl<sub>0.5</sub> could be fitted into three main peaks at 398.5, 399.9 and 401.0 eV (Figure 3c), which were assigned to sp<sup>2</sup>-hybridized nitrogen (C-N=C), tertiary nitrogen N-(C)<sub>3</sub> and free amino units (C-N-H), respectively [45]. The N 1s of CN was similar with that of CN-CoAl<sub>0.5</sub>, excepting for a shift of the peak responding to C-N=C at 398.4 eV. In Figure 3d, three pairs of peaks were detected for Co 2p spectra in both CN-CoAl<sub>0.5</sub> and CoAl-LDH. The main peaks at 781.1

and 783.9 eV of CoAl-LDH were assigned to  $\text{Co}^{3+}$  and  $\text{Co}^{2+}$ , respectively [46]. A slight shift towards low binding energy of  $\text{Co}^{2+}$  (783.8 eV) was observed for CN-CoAl<sub>0.5</sub>. In addition, the Al 2p spectra of both CN-CoAl<sub>0.5</sub> and CN were located at 74.0 eV (Figure 3e), confirming the Al<sup>3+</sup> in the samples. The O 1s spectra of CN-CoAl<sub>0.5</sub> and CN also showed no difference (Figure 3f). The predominant peak at 531.4 eV was attributed to the lattice oxygen, while the peak at 533.4 eV was assigned to the chemisorbed oxygen [47]. Thus, it is notable that there was an increase in the binding energy of N and decrease in  $\text{Co}^{2+}$  in the CN-CoAl<sub>0.5</sub> sample, as compared to that in CN and CoAl-LDH, while other elements showed analogous chemical states. This result suggests that a strong interaction between CoAl-LDH and CN was formed through the coordination of Co with N in the heterojunction.

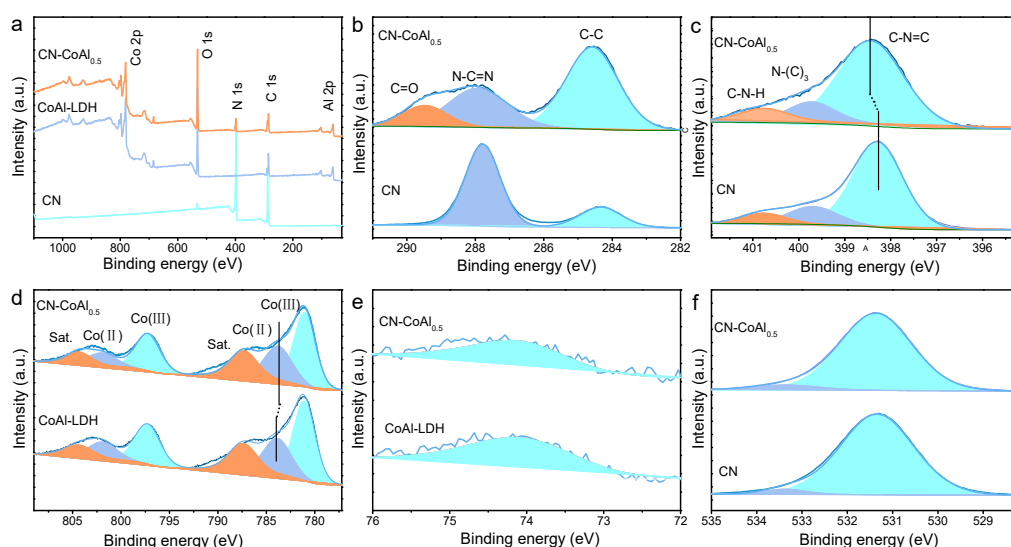


**Figure 3.** The survey spectra (a) and high-resolution XPS spectra of C (b), N (c), Co (d), Al (e), O (f) of CN-CoAl<sub>0.5</sub>, CN and CoAl-LDH.

The chemical structure of the CN-CoAl heterojunction and the interaction between the CoAl-LDH and CN components was further studied by an EPR and Raman spectra. As shown in Figure S2 (Supplementary Materials), bulk  $g\text{-C}_3\text{N}_4$  showed no EPR signal in the  $g$  range of 1.92–2.08. When bulk  $g\text{-C}_3\text{N}_4$  was exfoliated into 2D nanosheets, an obvious signal at  $g = 2.003$  for CN was observed (Figure 4a), corresponding to the unpaired electrons in  $\pi$ -bonded aromatic rings caused by C defects [48]. Notably, with the integration with CoAl-LDH, the peak was gradually intensified with the increasing amount of CoAl-LDH, which may be ascribed to the redistribution of  $\pi$ -electrons caused by the strong coordination of N with metal Co. The defect could serve as effective electron “traps” to accelerate the separation of photocarriers [49], thus benefiting the photocatalytic performance. Raman spectra of the as-prepared samples were recorded and are displayed in Figure 4b. The characteristic peaks of pure CN at 481, 592, 766, 874, 978 and 1119  $\text{cm}^{-1}$  were assigned to the C-N extended network, consistent with those obtained from pristine CN in the literature [50]. The Raman peak at 707  $\text{cm}^{-1}$  arose from the breathing mode of the s-triazine ring in  $g\text{-C}_3\text{N}_4$ , while the peak at 664  $\text{cm}^{-1}$  was associated with the heptazine ring structure of CN. The CN-CoAl heterojunctions displayed similar spectra as those of pure CN, suggesting the chemical structure of CN was preserved. However, the peak ascribed to the heptazine ring structure at 664  $\text{cm}^{-1}$  of CN-CoAl composites exhibited a slightly negative shift when compared to the spectrum of the bare CN, which may have been caused by the formation of a new chemical bond at the interface between  $g\text{-C}_3\text{N}_4$  and CoAl-LDH. The result well matched the FTIR and XPS analyses, consolidating the strong chemical interaction between CN and CoAl-LDH.

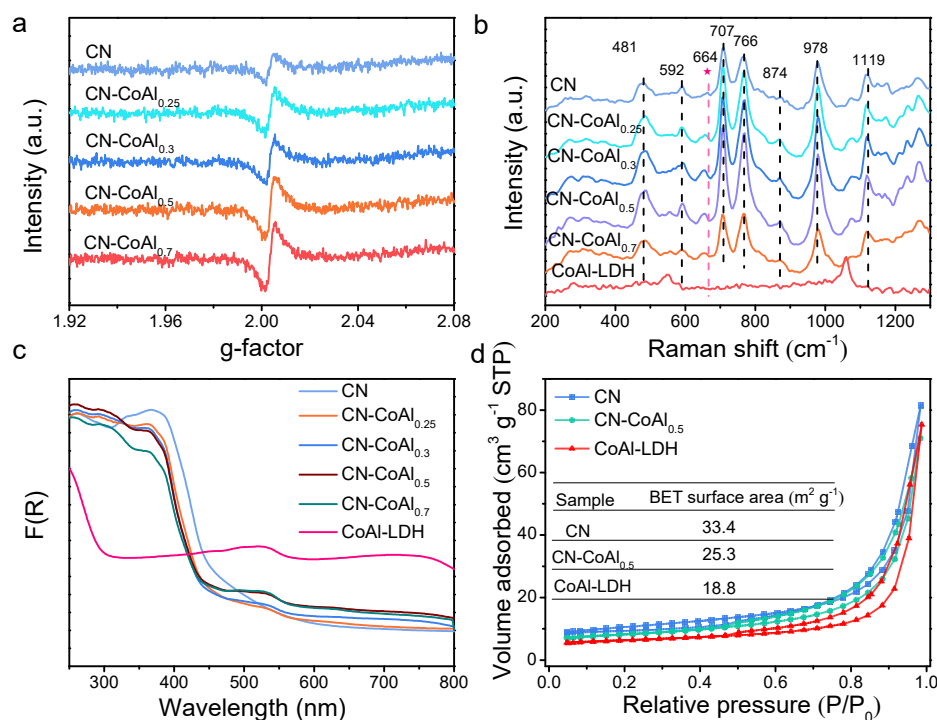


**Figure 4.** EPR (a), Raman (b), DRS (c) and BET (d) analyses of the prepared samples.

Furthermore, the optical absorption properties of the bare CN, CoAl-LDH and CN-CoAl<sub>x</sub> composites were measured by DRS. As shown in Figure 4c, the absorption edge of CN was around 480 nm, revealing its visible-light response characteristic. CoAl-LDH showed two distinct absorption peaks at 280 nm and in the range of 450–550 nm. The absorption edge at 280 nm was assigned to the ligand-to-metal charge transfer of CoAl-LDH, while the absorption at 530 nm was generated from d-d transitions of Co<sup>2+</sup> in an octahedral geometry [44,51]. As for the heterojunction composites, both characteristic peaks of the CN and CoAl-LDH were observed, suggesting the good integration of the two components in CN-CoAl<sub>x</sub>. Based on the transformed Kubelka–Munk function plots (Supplementary Materials, Figure S3), the band gaps ( $E_g$ ) of the CN and CoAl-LDH were measured to be 2.6 eV and 2.1 eV, respectively. Nitrogen (N<sub>2</sub>) adsorption–desorption measurements were measured to investigate the surface properties of the obtained catalysts. As presented in Figure 4d, all of the measured samples showed a type IV adsorption isotherm, revealing their mesoporous structure. The BET surface area of the CN, CN-CoAl<sub>0.5</sub> and CoAl-LDH were determined to be 33.4, 25.3 and 18.8 m<sup>2</sup> g<sup>−1</sup>, respectively. The CN-CoAl<sub>0.5</sub> showed a moderate surface area, which likely resulted from the hybridization of CN with CoAl-LDH.

The photocatalytic H<sub>2</sub> evolution activities of the as-prepared samples are presented in Figure 5a. No H<sub>2</sub> was detected after 4 h irradiation for pristine CoAl-LDH. In the case of bare CN, a relatively low H<sub>2</sub> production with the value of 233.2 μmol g<sup>−1</sup> was detected under visible light irradiation of 4 h, which should have been restricted by the fast recombination of the photogenerated electrons and holes. After coupling with CoAl-LDH, the photocatalytic H<sub>2</sub> production activities of the composites significantly increased. The optimal CN-CoAl<sub>0.5</sub> showed the highest H<sub>2</sub> evolution amount of 1952.9 μmol g<sup>−1</sup>, which is 8.4 times of CN. Moreover, the loading amount of the CoAl-LDH on g-C<sub>3</sub>N<sub>4</sub> played a significant role in the photocatalytic H<sub>2</sub> generation performance. With the increase in the CoAl-LDH content from 0.25 mmol to 0.5 mmol in the hybrids, the H<sub>2</sub> evolution rate enhanced gradually. The boosted photocatalytic activity may be due to the increased interacted interface and surface active sites in the heterojunction, which facilitated the separation of photogenerated carriers and promoted the surface reaction. However, a further increase in CoAl-LDH to 0.7 mmol depressed the H<sub>2</sub> evolution activity. This may

have been caused by the large amount of CoAl-LDH that shielded the light absorption of CN. The excessive loading of CoAl-LDH caused self-aggregation, which decreased the exposure of surface active sites, thus leading to a decline in the photocatalytic performance. XPS measurement of the as-prepared samples was performed to investigate the effect of the  $\text{Co}^{2+}/\text{Co}^{3+}$  ratio on photocatalytic activity. As shown in Figure S4 (Supplementary Materials), the Co species were in the form of a mixed state of +2 and +3 for all of the hybrid samples. By normalizing the peak areas, the atom ratios of  $\text{Co}^{2+}/\text{Co}^{3+}$  were calculated to be 2.11, 2.14, 2.07 and 2.01 for the CN-CoAl<sub>0.25</sub>, CN-CoAl<sub>0.3</sub>, CN-CoAl<sub>0.5</sub> and CN-CoAl<sub>0.7</sub>, respectively. The  $\text{Co}^{2+}/\text{Co}^{3+}$  ratios were almost the same for the different CN-CoAl samples, while their photocatalytic activities varied a lot. The result suggests that the  $\text{Co}^{2+}/\text{Co}^{3+}$  ratio was not a main factor in affecting the  $\text{H}_2$ -generation activity of the CN-CoAl composites.

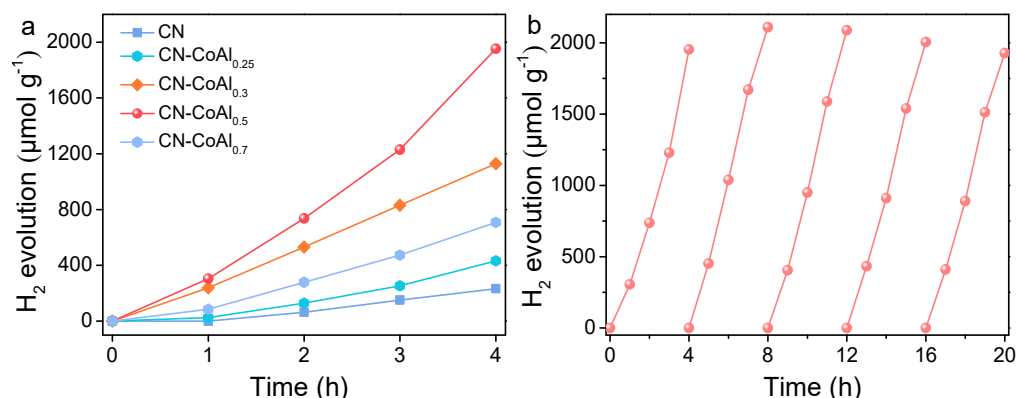


**Figure 5.** Photocatalytic hydrogen evolution over CN and CN-CoAl<sub>x</sub> (a), stability test of hydrogen evolution over CN-CoAl<sub>0.5</sub> (b).

For comparison, a reference catalyst of a CN/CoAl-Mix was also prepared by physical mixing of CN with CoAl-LDH. As shown in Figure S5 (Supplementary Materials), the  $\text{H}_2$  evolution rate of the CN/CoAl-Mix was slightly higher than the pure CN, while much lower than that of CN-CoAl<sub>0.5</sub>. The result directly proves that the construction of strong chemical bond interacted 2D/2D heterojunction is more effective for boosting the photocatalytic  $\text{H}_2$  production activity. The stability of photocatalytic  $\text{H}_2$  production over the optimized CN-CoAl<sub>0.5</sub> was also evaluated. As presented in Figure 5b, no obvious decrease in catalytic activity was observed during the five recycle tests. Moreover, the surface area and morphology of the CN-CoAl<sub>0.5</sub> after five cycles of stability test were investigated and are displayed in Figure S6 (Supplementary Materials). The BET surface area was measured to be  $28.1 \text{ m}^2 \text{ g}^{-1}$ , which was similar to the value before the reaction. The SEM and TEM images reveal that the 2D/2D sheet-to-sheet structure barely changed. These results verify that the 2D/2D CN-CoAl heterojunction had a satisfactory stability and reusability for photocatalytic  $\text{H}_2$  generation.

To gain mechanistic insight into the enhanced photoactivity of the CN-CoAl<sub>x</sub>, photoelectric responses of the heterojunction composites were carried out. Figure 6a shows the transient photocurrent test of the samples. The CoAl-LDH-modified CN samples exhibited much higher photocurrent strength compared to the CN, suggesting the constructed 2D/2D heterojunction with a large contact area could efficiently reduce the recombination rate of photogenerated carriers. The electrochemical impedance spectrum (EIS) results reveal that CN-CoAl<sub>0.5</sub> exhibited a decreased semicircle compared to the bare CN and CoAl-LDH (Figure 6b), illustrating that the 2D/2D interface strongly favored the migration of photogenerated charge carriers, and thus enhancing the photocatalytic  $\text{H}_2$  evolution activity. The behavior of photogenerated carriers was also monitored via PL spectra. As shown in Figure 6c, pure CN displayed an emission peak at around 470 nm. When the CoAl-LDH was introduced, the heterojunction showed a dramatically depressed PL inten-

sity, suggesting the inhibited recombination of photogenerated electron–hole pairs over the strong interacted heterojunction structure.

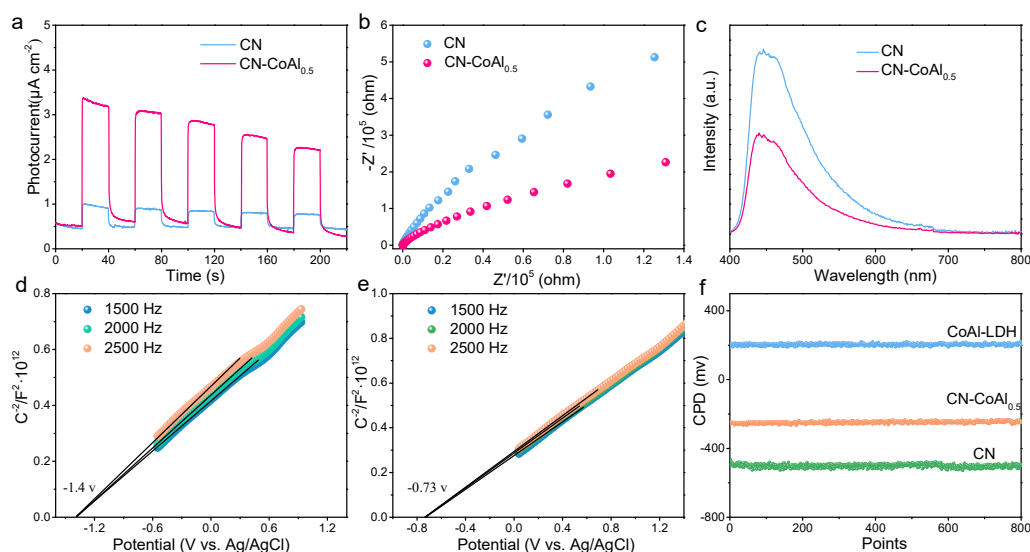


**Figure 6.** Transient photocurrent response (a), EIS (b), PL (c), Mott–Schottky plots of CN (d) and CoAl-LDH (e), CPDs of the as-prepared samples surface related to Au reference (f).

Moreover, the specific band structures of the CN and CoAl-LDH were determined by the Mott–Schottky test. As presented in Figure 6d,e, the spectra of both samples under three different constant frequencies showed a positive slope of the line segment, suggesting that the prepared CN and CoAl-LDH were typical n-type semiconductors. The derived values of the flat-band potentials ( $E_f$ ) of CN and CoAl-LDH were  $-1.4$  V and  $-0.73$  V (vs Ag/AgCl) at pH 7, respectively. According to the conversion equation of  $E_{\text{NHE}} = E_{\text{Ag/AgCl}} + E^0_{\text{Ag/AgCl}}$ , ( $E^0_{\text{Ag/AgCl}}$  is about 0.197 V at 25 °C, pH = 7),  $E_f$  of CN and CoAl-LDH were determined to be  $-1.20$  V and  $-0.53$  V versus the normal hydrogen electrode (NHE, pH = 7). Thereby, the valence band (VB) of CN and CoAl-LDH could be calculated to be 1.40 V and 1.57 V. Furthermore, the Kelvin probe test was measured to study the interfacial electronic structure. Figure 6f depicts the measured contact potential difference (CPDs) of the as-prepared samples related to the Au (5.1 eV) reference. The work function of the CN CoAl-LDH and CN-CoAl<sub>0.5</sub> were calculated to be 4.62 eV, 5.4 eV and 4.85 eV, respectively.

Based on the above analysis, a plausible photogenerated charge carrier transfer mechanism over the CN-CoAl heterojunction could be proposed. As shown in Figure 7a, due to the lower Fermi level of CoAl-LDH than that of CN, free electrons transferred from CN to CoAl-LDH through the N–metal bond until an equilibrium state formed (Figure 7b). As such, an interfacial electric field oriented in the direction from the CN to CoAl-LDH emerged. Under light irradiation, both CN and CoAl-LDH could be photoexcited to generate electron–hole pairs. With the driving force of the built-in electric field, photogenerated electrons from the CB of CoAl-LDH transferred to the VB of CN and recombined with the holes (Figure 7c), thus realizing the Z-scheme charge transfer. Concurrently, the accumulated electrons on the CB of CN reacted with H<sub>2</sub>O for H<sub>2</sub> production, while the holes of CoAl-LDH were trapped by TEOA.

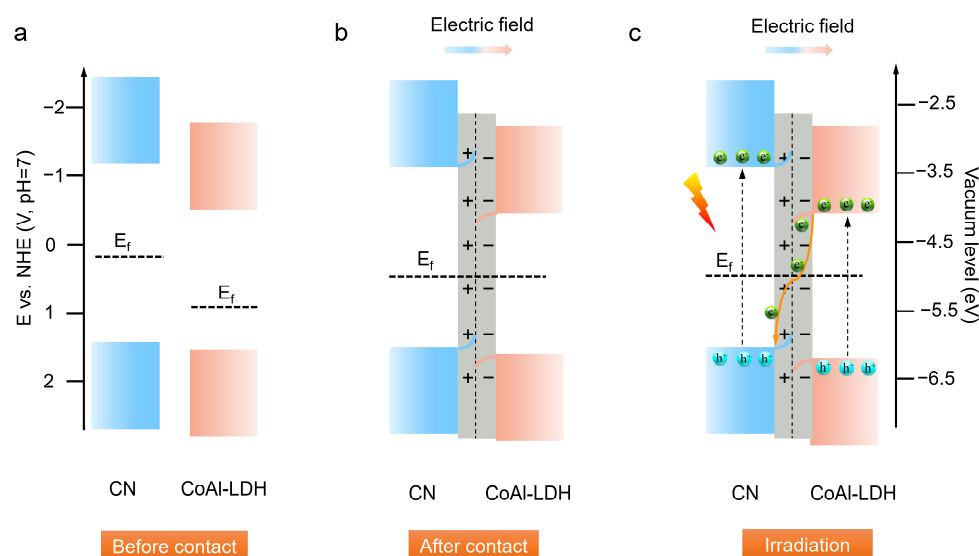


**Figure 7.** Schematic diagram for band structure of CN and CoAl-LDH before contact (a), after contact (b) and the light-induced charge transfer from CN to CoAl-LDH toward  $H_2$  evolution (c).

#### 4. Conclusions

In summary, a 2D/2D organic/inorganic g- $C_3N_4$ /CoAl-LDH heterojunction with a strong interacted interface was synthesized via an in situ hydrothermal method. The resulting composites showed a markedly improved photocatalytic  $H_2$  production activity. The optimal CN-CoAl composite displayed a  $H_2$  evolution of  $1952.9 \mu\text{mol g}^{-1}$  for 4 h visible light irradiation, which is 8.4 times as that of pure CN. The enhanced photocatalytic activity crucially relied on the well-matched band positions of g- $C_3N_4$  and CoAl-LDH components, as well as the sufficient interfacial contact between them, which greatly benefited the migration and separation of the photogenerated charge carriers.

**Supplementary Materials:** The following are available online at <https://www.mdpi.com/article/10.3390/nano11102762/s1>. Figure S1: SEM image of the prepared CN-CoAl<sub>0.7</sub>. Figure S2: EPR spectra of bulk g- $C_3N_4$ , CN and CoAl-LDH. Figure S3: Tauc plots of CN and CoAl-LDH. Figure S4: XPS spectra of Co in CN-CoAl<sub>x</sub> samples. Figure S5: Photocatalytic  $H_2$  evolution rates of CoAl-LDH, CN, CN/CoAl-Mix and CN-CoAl<sub>0.5</sub>. Figure S6: BET (a), SEM (b) and TEM (c) analyses of CN-CoAl<sub>0.5</sub> after 5 cycles of  $H_2$ -generation stability text.

**Author Contributions:** Y.X.: Conceptualization, Methodology, Data Curation, Writing—Reviewing. R.L.: Investigation, Data curation. M.-Q.Y.: Resources, Writing—Reviewing and Editing. S.Z.: Conceptualization, Writing—Reviewing and Editing. G.Y.: Resources, Supervision. All authors have read and agreed to the published version of the manuscript.

**Funding:** This work was financially supported by the National Natural Science Foundation of China (22108129, 21806085, 21902030), Natural Science Foundation of Fujian Province (2020J05223, 2019J01016), Natural Science Foundation of Ningde Normal University (2019Y07, 2019Q101, 2020T01) and Middle-Aged Teacher Education Project of Fujian Provincial Department of Education (JAT190808).

**Conflicts of Interest:** The authors declare no conflict of interest.

#### References

1. Yang, M.; Shen, L.; Lu, Y.; Chee, S.W.; Lu, X.; Chi, X.; Chen, Z.; Xu, Q.; Mirsaidov, U.; Ho, G.W. Disorder engineering in monolayer nanosheets enabling photothermal catalysis for full solar spectrum (250–2500 nm) harvesting. *Angew. Chem. Int. Ed.* **2019**, *58*, 3077–3081. [[CrossRef](#)]
2. Zhang, Y.C.; Afzal, N.; Pan, L.; Zhang, X.; Zou, J.J. Structure-activity relationship of defective metal-based photocatalysts for water splitting: Experimental and theoretical perspectives. *Adv. Sci.* **2019**, *6*, 1900053. [[CrossRef](#)] [[PubMed](#)]
3. Li, C.; Xu, Y.; Tu, W.; Chen, G.; Xu, R. Metal-free photocatalysts for various applications in energy conversion and environmental purification. *Green Chem.* **2017**, *19*, 882–899. [[CrossRef](#)]

4. Wang, Z.; Li, C.; Domen, K. Recent developments in heterogeneous photocatalysts for solar-driven overall water splitting. *Chem. Soc. Rev.* **2019**, *48*, 2109–2125. [[CrossRef](#)]
5. Lu, Q.; Yu, Y.; Ma, Q.; Chen, B.; Zhang, H. 2D transition-metal-dichalcogenide-nanosheet-based composites for photocatalytic and electrocatalytic hydrogen evolution reactions. *Adv. Mater.* **2016**, *28*, 1917–1933. [[CrossRef](#)] [[PubMed](#)]
6. Yin, S.; Liu, S.; Yuan, Y.; Guo, S.; Ren, Z. Octahedral shaped PbTiO<sub>3</sub>-TiO<sub>2</sub> nanocomposites for high-efficiency photocatalytic hydrogen production. *Nanomaterials* **2021**, *11*, 2295. [[CrossRef](#)]
7. Martino, M.; Ruocco, C.; Meloni, E.; Pullumbi, P.; Palma, V. Main hydrogen production processes: An overview. *Catalyst* **2021**, *11*, 547. [[CrossRef](#)]
8. Zhou, W.; Li, W.; Wang, J.Q.; Qu, Y.; Yang, Y.; Xie, Y.; Zhang, K.; Wang, L.; Fu, H.; Zhao, D. Ordered mesoporous black TiO<sub>2</sub> as highly efficient hydrogen evolution photocatalyst. *J. Am. Chem. Soc.* **2014**, *136*, 9280–9283. [[CrossRef](#)]
9. Geng, R.; Yin, J.; Zhou, J.; Jiao, T.; Feng, Y.; Zhang, L.; Chen, Y.; Bai, Z.; Peng, Q. In situ construction of Ag/TiO<sub>2</sub>/g-C<sub>3</sub>N<sub>4</sub> heterojunction nanocomposite based on hierarchical co-assembly with sustainable hydrogen Evolution. *Nanomaterials* **2020**, *10*, 1. [[CrossRef](#)]
10. Sajan, C.P.; Wageh, S.; Al-Ghamdi, A.A.; Yu, J.; Cao, S. TiO<sub>2</sub> nanosheets with exposed {001} facets for photocatalytic applications. *Nano Res.* **2015**, *9*, 3–27. [[CrossRef](#)]
11. Zhang, P.; Wang, T.; Gong, J. Mechanistic understanding of the plasmonic enhancement for solar water splitting. *Adv. Mater.* **2015**, *27*, 5328–5342. [[CrossRef](#)]
12. Meng, A.; Wu, S.; Cheng, B.; Yu, J.; Xu, J. Hierarchical TiO<sub>2</sub>/Ni(OH)<sub>2</sub> composite fibers with enhanced photocatalytic CO<sub>2</sub> reduction performance. *J. Mater. Chem. A* **2018**, *6*, 4729–4736. [[CrossRef](#)]
13. Jia, J.; Sun, W.; Zhang, Q.; Zhang, X.; Hu, X.; Liu, E.; Fan, J. Inter-plane heterojunctions within 2D/2D FeSe<sub>2</sub>/g-C<sub>3</sub>N<sub>4</sub> nanosheet semiconductors for photocatalytic hydrogen generation. *Appl. Catal. B* **2020**, *261*, 118249. [[CrossRef](#)]
14. Che, W.; Cheng, W.; Yao, T.; Tang, F.; Liu, W.; Su, H.; Huang, Y.; Liu, Q.; Liu, J.; Hu, F.; et al. Fast photoelectron transfer in (cring)-C<sub>3</sub>N<sub>4</sub> plane heterostructural nanosheets for overall water splitting. *J. Am. Chem. Soc.* **2017**, *139*, 3021–3026. [[CrossRef](#)]
15. Ran, J.; Guo, W.; Wang, H.; Zhu, B.; Yu, J.; Qiao, S.Z. Metal-free 2D/2D Phosphorene/g-C<sub>3</sub>N<sub>4</sub> Van der Waals heterojunction for highly enhanced visible-light photocatalytic H<sub>2</sub> production. *Adv. Mater.* **2018**, *30*, e1800128. [[CrossRef](#)] [[PubMed](#)]
16. Wang, S.; Wang, Y.; Zhang, S.L.; Zang, S.Q.; Lou, X.W.D. Supporting ultrathin ZnIn<sub>2</sub>S<sub>4</sub> nanosheets on Co/N-doped graphitic carbon nanocages for efficient photocatalytic H<sub>2</sub> generation. *Adv. Mater.* **2019**, *31*, 1903404. [[CrossRef](#)]
17. Yang, M.; Xu, Y.; Lu, W.; Zeng, K.; Zhu, H.; Xu, Q.; Ho, W. Self-surface charge exfoliation and electrostatically coordinated 2D hetero-layered hybrids. *Nat. Commun.* **2017**, *8*, 1–9. [[CrossRef](#)] [[PubMed](#)]
18. Lian, J.; Li, D.; Qi, Y.; Yang, N.; Zhang, R.; Xie, T.; Guan, N.; Li, L.; Zhang, F. Metal-seed assistant photodeposition of platinum over Ta<sub>3</sub>N<sub>5</sub> photocatalyst for promoted solar hydrogen production under visible light. *J. Energy Chem.* **2021**, *55*, 444–448. [[CrossRef](#)]
19. Zuo, Q.; Liu, T.; Chen, C.; Ji, Y.; Gong, X.; Mai, Y.; Zhou, Y. Ultrathin metal-organic framework nanosheets with ultrahigh loading of single Pt atoms for efficient visible-light-driven photocatalytic H<sub>2</sub> evolution. *Angew. Chem. Int. Ed.* **2019**, *58*, 10198–10203. [[CrossRef](#)]
20. Liang, R.; Huang, R.; Ying, S.; Wang, X.; Yan, G.; Wu, L. Facile in situ growth of highly dispersed palladium on phosphotungstic-acid-encapsulated MIL-100(Fe) for the degradation of pharmaceuticals and personal care products under visible light. *Nano Res.* **2017**, *11*, 1109–1123. [[CrossRef](#)]
21. Zhang, F.M.; Sheng, J.L.; Yang, Z.D.; Sun, X.J.; Tang, H.L.; Lu, M.; Dong, H.; Shen, F.C.; Liu, J.; Lan, Y.Q. Rational design of MOF/COF hybrid materials for photocatalytic H<sub>2</sub> evolution in the Presence of Sacrificial Electron Donors. *Angew. Chem. Int. Ed.* **2018**, *57*, 12106–12110. [[CrossRef](#)]
22. Cheng, C.; He, B.; Fan, J.; Cheng, B.; Cao, S.; Yu, J. An inorganic/organic s-scheme heterojunction H<sub>2</sub>-production photocatalyst and its charge transfer mechanism. *Adv. Mater.* **2021**, *33*, 2100317. [[CrossRef](#)] [[PubMed](#)]
23. Wang, Z.; Lin, Z.; Shen, S.; Zhong, W.; Cao, S. Advances in designing heterojunction photocatalytic materials. *Chin. J. Catal.* **2021**, *42*, 710–730. [[CrossRef](#)]
24. Xue, C.; An, H.; Shao, G.; Yang, G. Accelerating directional charge separation via built-in interfacial electric fields originating from work-function differences. *Chin. J. Catal.* **2021**, *42*, 583–594. [[CrossRef](#)]
25. Xia, Y.; Chen, W.; Liang, S.; Bi, J.; Wu, L.; Wang, X. Engineering a highly dispersed co-catalyst on a few-layered catalyst for efficient photocatalytic H<sub>2</sub> evolution: A case study of Ni(OH)<sub>2</sub>/HNb<sub>3</sub>O<sub>8</sub> nanocomposites. *Catal. Sci. Technol.* **2017**, *7*, 5662–5669. [[CrossRef](#)]
26. Chen, J.; Zhan, J.; Zhang, Y.; Tang, Y. Construction of a novel ZnCo<sub>2</sub>O<sub>4</sub>/Bi<sub>2</sub>O<sub>3</sub> heterojunction photocatalyst with enhanced visible light photocatalytic activity. *Chin. Chem. Lett.* **2019**, *30*, 735–738. [[CrossRef](#)]
27. Zheng, Y.; Fan, M.; Li, K.; Zhang, R.; Li, X.; Zhang, L.; Qiao, Z.-A. Ultraviolet-induced Ostwald ripening strategy towards a mesoporous Ga<sub>2</sub>O<sub>3</sub>/GaOOH heterojunction composite with a controllable structure for enhanced photocatalytic hydrogen evolution. *Catal. Sci. Technol.* **2020**, *10*, 2882–2892. [[CrossRef](#)]
28. Wu, S.; Yu, X.; Zhang, J.; Zhang, Y.; Zhu, Y.; Zhu, M. Construction of BiOCl/CuBi<sub>2</sub>O<sub>4</sub> S-scheme heterojunction with oxygen vacancy for enhanced photocatalytic diclofenac degradation and nitric oxide removal. *Chem. Eng. J.* **2021**, *411*, 128555. [[CrossRef](#)]
29. Geng, Y.; Chen, D.; Li, N.; Xu, Q.; Li, H.; He, J.; Lu, J. Z-Scheme 2D/2D α-Fe<sub>2</sub>O<sub>3</sub>/g-C<sub>3</sub>N<sub>4</sub> heterojunction for photocatalytic oxidation of nitric oxide. *Appl. Catal. B* **2021**, *280*, 119409. [[CrossRef](#)]
30. He, F.; Meng, A.; Ho, W.; Yu, J. Enhanced photocatalytic H<sub>2</sub>-production activity of WO<sub>3</sub>/TiO<sub>2</sub> step-scheme heterojunction by graphene modification. *Chin. J. Catal.* **2020**, *41*, 9–20. [[CrossRef](#)]

31. Xia, Y.; Liang, S.; Wu, L.; Wang, X. Ultrasmall NiS decorated HNb<sub>3</sub>O<sub>8</sub> nanosheets as highly efficient photocatalyst for H<sub>2</sub> evolution reaction. *Catal. Today* **2019**, *330*, 195–202. [[CrossRef](#)]
32. Feng, N.; Lin, H.; Deng, F.; Ye, J. Interfacial-bonding Ti-N-C boosts efficient photocatalytic H<sub>2</sub> evolution in close coupling g-C<sub>3</sub>N<sub>4</sub>/TiO<sub>2</sub>. *J. Phys. Chem. C* **2021**, *125*, 12012–12018. [[CrossRef](#)]
33. Xia, M.; Yan, X.; Li, H.; Wells, N.; Yang, G. Well-designed efficient charge separation in 2D/2D N doped La<sub>2</sub>Ti<sub>2</sub>O<sub>7</sub>/ZnIn<sub>2</sub>S<sub>4</sub> heterojunction through band structure/morphology regulation synergistic effect. *Nano Energy* **2020**, *78*, 105401. [[CrossRef](#)]
34. Wang, X.; Wang, X.; Huang, J.; Li, S.; Meng, A.; Li, Z. Interfacial chemical bond and internal electric field modulated Z-scheme Sv-ZnIn<sub>2</sub>S<sub>4</sub>/MoSe<sub>2</sub> photocatalyst for efficient hydrogen evolution. *Nat. Commun.* **2021**, *12*, 4112. [[CrossRef](#)] [[PubMed](#)]
35. Xia, Y.; Zhu, S.; Liang, R.; Huang, R.; Yan, G.; Liang, S. Interfacial reconstruction of 2D/2D ZnIn<sub>2</sub>S<sub>4</sub>/HNb<sub>3</sub>O<sub>8</sub> through Nb-S bonds for efficient photocatalytic H<sub>2</sub> evolution performance. *Mater. Des.* **2021**, *209*, 110007. [[CrossRef](#)]
36. Qi, Y.; Jiang, J.; Liang, X.; Ouyang, S.; Mi, W.; Ning, S.; Zhao, L.; Ye, J. Fabrication of black In<sub>2</sub>O<sub>3</sub> with dense oxygen vacancy through dual functional carbon doping for enhancing photothermal CO<sub>2</sub> hydrogenation. *Adv. Funct. Mater.* **2021**, *31*, 2100908. [[CrossRef](#)]
37. Liang, X.; Wang, P.; Gao, Y.; Huang, H.; Tong, F.; Zhang, Q.; Wang, Z.; Liu, Y.; Zheng, Z.; Dai, Y.; et al. Design and synthesis of porous M-ZnO/CeO<sub>2</sub> microspheres as efficient plasmonic photocatalysts for nonpolar gaseous molecules oxidation: Insight into the role of oxygen vacancy defects and M=Ag, Au nanoparticles. *Appl. Catal. B* **2020**, *260*, 118151. [[CrossRef](#)]
38. Chen, X.; Li, J.-Y.; Tang, Z.-R.; Xu, Y.-J. Surface-defect-engineered photocatalyst for nitrogen fixation into value-added chemical feedstocks. *Catal. Sci. Technol.* **2020**, *10*, 6098–6110. [[CrossRef](#)]
39. Chen, L.; Zhu, D.; Li, J.; Wang, X.; Zhu, J.; Francis, P.S.; Zheng, Y. Sulfur and potassium co-doped graphitic carbon nitride for highly enhanced photocatalytic hydrogen evolution. *Appl. Catal. B* **2020**, *273*, 119050. [[CrossRef](#)]
40. Wang, D.; Zeng, H.; Xiong, X.; Wu, M.-F.; Xia, M.; Xie, M.; Zou, J.-P.; Luo, S.-L. Highly efficient charge transfer in CdS-covalent organic framework nanocomposites for stable photocatalytic hydrogen evolution under visible light. *Sci. Bull.* **2020**, *65*, 113–122. [[CrossRef](#)]
41. Wang, X.; Maeda, K.; Thomas, A.; Takanabe, K.; Xin, G.; Carlsson, J.M.; Domen, K.; Antonietti, M. A metal-free polymeric photocatalyst for hydrogen production from water under visible light. *Nat. Mater.* **2009**, *8*, 76–80. [[CrossRef](#)] [[PubMed](#)]
42. Lin, Q.; Li, L.; Liang, S.; Liu, M.; Bi, J.; Wu, L. Efficient synthesis of monolayer carbon nitride 2D nanosheet with tunable concentration and enhanced visible-light photocatalytic activities. *Appl. Catal. B* **2015**, *163*, 135–142. [[CrossRef](#)]
43. Zhang, S.; Si, Y.; Li, B.; Yang, L.; Dai, W.; Luo, S. Atomic-level and modulated interfaces of photocatalyst heterostructure constructed by external defect-induced strategy: A critical review. *Small* **2021**, *17*, e2004980. [[CrossRef](#)]
44. Jo, W.K.; Tonda, S. Novel CoAl-LDH/g-C<sub>3</sub>N<sub>4</sub>/RGO ternary heterojunction with notable 2D/2D/2D configuration for highly efficient visible-light-induced photocatalytic elimination of dye and antibiotic pollutants. *J. Hazard. Mater.* **2019**, *368*, 778–787. [[CrossRef](#)] [[PubMed](#)]
45. Li, C.; Du, Y.; Wang, D.; Yin, S.; Tu, W.; Chen, Z.; Kraft, M.; Chen, G.; Xu, R. Unique P-Co-N surface bonding states constructed on g-C<sub>3</sub>N<sub>4</sub> nanosheets for drastically enhanced photocatalytic activity of H<sub>2</sub> evolution. *Adv. Funct. Mater.* **2017**, *27*, 1604328. [[CrossRef](#)]
46. Ping, J.; Wang, Y.; Lu, Q.; Chen, B.; Chen, J.; Huang, Y.; Ma, Q.; Tan, C.; Yang, J.; Cao, X.; et al. Self-assembly of single-layer CoAl-layered double hydroxide nanosheets on 3D graphene network used as highly efficient electrocatalyst for oxygen evolution reaction. *Adv. Mater.* **2016**, *28*, 7640–7645. [[CrossRef](#)] [[PubMed](#)]
47. Wu, Y.; Wang, H.; Sun, Y.; Xiao, T.; Tu, W.; Yuan, X.; Zeng, G.; Li, S.; Chew, J.W. Photogenerated charge transfer via interfacial internal electric field for significantly improved photocatalysis in direct Z-scheme oxygen-doped carbon nitrogen/CoAl-layered double hydroxide heterojunction. *Appl. Catal. B* **2018**, *227*, 530–540. [[CrossRef](#)]
48. Cao, S.; Fan, B.; Feng, Y.; Chen, H.; Jiang, F.; Wang, X. Sulfur-doped g-C<sub>3</sub>N<sub>4</sub> nanosheets with carbon vacancies: General synthesis and improved activity for simulated solar-light photocatalytic nitrogen fixation. *Chem. Eng. J.* **2018**, *353*, 147–156. [[CrossRef](#)]
49. Duan, L.; Li, G.; Zhang, S.; Wang, H.; Zhao, Y.; Zhang, Y. Preparation of S-doped g-C<sub>3</sub>N<sub>4</sub> with C vacancies using the desulfurized waste liquid extracting salt and its application for NO<sub>x</sub> removal. *Chem. Eng. J.* **2021**, *411*, 128551. [[CrossRef](#)]
50. Hu, S.; Yang, L.; Tian, Y.; Wei, X.; Ding, J.; Zhong, J.; Chu, P. Simultaneous nanostructure and heterojunction engineering of graphitic carbon nitride via in situ Ag doping for enhanced photoelectrochemical activity. *Appl. Catal. B* **2015**, *163*, 611–622. [[CrossRef](#)]
51. Dou, Y.; Zhang, S.; Pan, T.; Xu, S.; Zhou, A.; Pu, M.; Yan, H.; Han, J.; Wei, M.; Evans, D.G.; et al. TiO<sub>2</sub>@layered double hydroxide core-shell nanospheres with largely enhanced photocatalytic activity toward O<sub>2</sub> generation. *Adv. Funct. Mater.* **2015**, *25*, 2243–2249. [[CrossRef](#)]